PERIODICO di MINERALOGIA
established in 1930

DIPARTIMENTO DI SCIENZE DELLA TERRA
SAPIENZA UNIVERSITÀ DI ROMA

An International Journal of
Mineralogy, Crystallography, Geochemistry,
Ore Deposits, Petrology, Volcanology
and applied topics on Environment, Archaeometry and Cultural Heritage

Crystal-chemical effects of heat treatment on Cr- and V-bearing Ca-dominant green tourmalines (fluor-uvite, magnesio-lucchesiite)

Peter Bačík [1,2,*], Petra Kardošová [1], Jana Fridrichová [1], Olena Rybnikova [1], Radek Škoda [3]

[1] Comenius University in Bratislava, Faculty of Natural Sciences, Department of Mineralogy and Petrology, Mlynská dolina, 842 15 Bratislava, Slovak Republic
[2] Earth Science Institute of the Slovak Academy of Sciences, Dúbravská cesta 9, P.O. BOX 106, 84005 Bratislava, Slovakia
[3] Masaryk University, Department of Geological Sciences, Kotlářská 2, 611 37 Brno, Czech Republic

ARTICLE INFO

Submitted: May 2024
Accepted: August 2024
Available on line: September 2024

* Corresponding author:
peter.bacik@uniba.sk

Doi: 10.13133/2239-1002/18524

How to cite this article:
Bačík P. et al. (2024)
Period. Mineral. 93, 147-164

ABSTRACT

We present a detailed study of thermally driven changes in Ca-dominant tourmaline using Electron Probe Microanalysis (EPMA), powder X-ray diffraction (PXRD), Raman and optical absorption spectroscopy (OAS). The KEN samples from Kenya (5 crystal fragments) can be classified as fluor-uvite, while TAN from Tanzania (5 fragments) is dominantly magnesio-lucchesiite. Tourmaline samples were thermally treated in air at 700, 800, 900, and 1000 °C. Both sets were green with different hues, TAN with a bluer hue than KEN. After heating, no significant visual changes were observed in TAN samples until breakdown at 1000 °C. In KEN, after heating at 700 °C, the yellowish tint disappeared. Raman spectroscopy showed no significant changes after heating. Raman luminescence spectra revealed the sharp intensive band located at 680-684 nm, accompanied by a broad band between 690 and 900 nm in all samples heated up to 900 °C. OAS spectra look similar, with two major bands in blue and yellow to red regions. In TAN, the bands shift with the increasing Cr/V from 608 to 604 nm. In KEN with low Cr/V, the band is located between 613-617 nm. After heating at 1000 °C, both samples broke down with different associations: cordierite/indialite and glass from magnesio-lucchesiite, and cordierite/indialite, mullite-like phase, spinel and glass from fluor-uvite. There was a difference in volume between the samples; both samples expanded in volume, but the KEN sample expanded more with larger pores likely resulting from a higher proportion of volatile phase in this sample.

Keywords: tourmaline; fluor-uvite; magnesio-lucchesiite; heat treatment; structural breakdown.

INTRODUCTION

Although high-temperature behaviour has been investigated on tourmalines of various compositions, experiments on calcium tourmalines have not received significant attention. The occurrence of Ca-rich tourmalines in nature has been experimentally demonstrated as a function of pressure, temperature, and composition of metamorphic fluids (Berryman et al., 2016), but calcic tourmalines remain so far less investigated in terms of thermal behaviour, dehydration and breakdown products, partly because uvite was only recently officially approved a new mineral species of tourmaline supergroup (Bosi et al., 2022).

Experimentally, uvite was studied from San Piero in Campo (Island of Elba, Italy) by in situ high-temperature powder X-ray diffraction (HT-PXRD) up to the structural

breakdown (Ballirano et al., 2022b). Changes in the structural parameters (unit cell parameters and average bond lengths) were monitored along with position occupancy, and a heat-induced Fe oxidation process compensated by $(OH)^-$ deprotonation was observed, starting at 450 °C and ending at 650 °C. The uvite decomposition reaction takes place between 800 and 900 °C. The breakdown products were identified at room temperature by PXRD, and the breakdown reaction can be described as follows: tourmaline → indialite + yuanfuliite + plagioclase + "boromullite" phase + hematite (Ballirano et al., 2022b). The observed assemblage of phases is significantly different with respect to the thermal breakdown of both Fe-rich fluor-elbaite (Celata et al., 2021) and Mn-rich fluor-elbaite (Ballirano et al., 2022a). In particular, the mullite-structured phase reported as the prevailing crystalline product of Fe-bearing fluor-elbaite and Mn-rich fluor-elbaite breakdown is replaced by indialite (Ballirano et al., 2022b).

We present a detailed study of thermally driven changes in Ca-dominant tourmalines with different mineral compositions (fluor-uvite and magnesio-lucchesiite) and content of V and Cr, which are the dominant chromophores causing green colour of both samples. High-temperature changes were evidenced using Electron Probe Microanalysis (EPMA), powder X-ray diffraction (PXRD), Raman and optical absorption spectroscopy (OAS). Tourmaline samples were thermally treated in air at 700, 800, 900, and 1000 °C.

CALCIUM-DOMINANT TOURMALINES

Tourmalines can be divided into three groups: alkali, calcic, and *X*-vacant tourmaline subgroup (Henry et al., 2011). Our studied tourmalines belong to the calcic group, which has fluor-uvite and magnesio-lucchesiite compositions. These tourmalines are a common component of calcic metasediments such as calcareous rocks and marbles (Henry and Guidotti, 1985).

Tourmaline is stable under various geologic conditions, including those where crustal material is recycled through subduction zones to the upper mantle (Henry and Dutrow, 1996; Ota et al., 2008a, 2008b; Shimizu and Ogasawara, 2013). Tourmaline can also form in a subduction environment in presence of B-bearing fluid. When the other phases of paragenesis together with tourmaline reach their breakdown conditions, and some elements are recycled in tourmaline structure (which is stable at those depths), it can form or grow (if it already existed in the recycled material) with a new composition depending on the elements that were available to be incorporated. At greater depths, the tourmaline itself experiences breakdown and water fluids are released, which can escape again and metasomatize the surrounding rocks, reducing both their solidus temperature and the viscosity of possibly associated melt (Pichavant, 1981; Dingwell et al., 1992).

When the subducting serpentinites are closely associated with carbonaceous (meta)sediments, the release of Ca-rich metasomatic fluids along the lithospheric slab may occur as a consequence of dehydration reactions leading, for example, to form strongly Ca-enriched patches and layers of hybrid rocks (lawsonite-bearing) in metagabbro matrix (Tartarotti et al., 2019). Those Ca-rich metasomatic fluids may also lead to the formation of Ca-bearing tourmaline, which acts as a calcium carrier at greater depths until breakdown conditions are reached. In some cases, tourmaline can experience an extreme chemical evolution, manifested by a change in its composition, for example, from alkali to calcic (Henry and Dutrow, 1990).

Fluor-uvite

Fluor-uvite was first found in 1929 in Uva Province, Sri Lanka, hence the name. The mineral is sought after by collectors because of its pronounced colours and often large crystal size.

Fluor-uvite is an end member of the tourmaline supergroup with the chemical formula $CaMg_3(Al_5Mg)(Si_6O_{18})(BO_3)_3(OH)_3F$. It is a rare mineral found in Ca-rich contact metamorphic rocks with increased amounts of boron (MacDonald and Hawthorne, 1995). Uvite substitution $CaMg(NaAl)_{-1}$ is the most common and most likely mechanism of incorporation of Ca within the uvite molecule into the tourmaline structure. It is typical for tourmalines with a low Li content. Another possible mechanism for the entry of Ca into the *X* site is the substitution $^{X}Ca+^{Y}Mg+^{W}O^{2-}\leftrightarrow{}^{X}\square+{}^{Y}Al+{}^{W}OH^{-}$ (Henry and Dutrow, 1990). In Li-bearing tourmalines, the more usual is the model of liddicoatite substitution $^{X}Na+^{Y}Al\leftrightarrow{}^{X}Ca+^{Y}Li$ (Henry and Guidotti, 1985).

Magnesio-lucchesiite

Magnesio-lucchesiite is a mineral species with the general structural formula $CaMg_3Al_6(Si_6O_{18})(BO_3)_3(OH)_3O$. The holotype material was discovered within a lamprophyre dike that crosscuts tourmaline-bearing metapelites in the exocontact of the O'Grady Batholith, Northwest Territories (Canada). Two other samples were found at San Piero in Campo, Elba Island, Tuscany (Italy), in hydrothermal veins embedded in metaserpentinites within the contact aureole of the Monte Capanne intrusion.

Magnesio-lucchesiite is an oxy species belonging to the calcium group of the tourmaline supergroup. It is related to lucchesiite by the homovalent substitution $^{Y}Fe\leftrightarrow{}^{Y}Mg$ and to feruvite by the homovalent and heterovalent substitutions $^{Y}Fe\leftrightarrow{}^{Y}Mg$ and $^{Z}Al^{3+}+{}^{W}O^{2-}\leftrightarrow{}^{Z}Mg^{2+}+$

$^{W}(OH)^{-}$. Occurrences of magnesio-lucchesiite show that its presence is not limited only to the replacement of mafic minerals; it may also form in metacarbonate rocks by fluctuations of F and Al during the crystallisation of common uvitic tourmaline. High miscibility with other tourmaline end members indicates a great petrogenetic potential of magnesio-lucchesiite in Mg, Al-rich calc-silicate rocks, as well as contact-metamorphic and metasomatic rocks (Scribner et al., 2021).

CHROMIUM AND VANADIUM IN TOURMALINE

In the structure of studied fluor-uvite and magnesio-lucchesite, there are incorporated elements such as Cr and V. Vanadium and chromium cations usually occupy the *Z* octahedral sites of tourmaline. When their contents are higher than 3.00 apfu (more than 50% of the position), they form the end members of the tourmaline group, Cr in chrome-dravite and V in vanadium-dravite (Rumyantseva, 1983; Bosi et al., 2012, 2014, 2017). The mechanism of this process is simple - $^{Z}Al \leftrightarrow (^{Z}Cr^{3+}, {}^{Z}V^{3+})$ (Bosi et al., 2004). However, part of V and Cr can also enter the *Y* site (Henry et al., 2011); Cr in the dravite-chromium-dravite series even preferentially and forms an antagonistic pair with Mg, which, on the other hand, prefers the *Z* octahedron (Bosi et al., 2004). The mechanism for the entry of Cr and V into *Y* could be $^{Y}Mg + {}^{Z}Al \leftrightarrow {}^{Y}Cr + {}^{Z}Mg$ (Bosi et al., 2004).

SAMPLES

The studied samples come from two famous localities in Kenya and Tanzania and are usually commercially distributed as "chromdravite".

The sample from Kenya (hereinafter abbreviated as KEN) originates from Taita hills in the Mwatate Quadrangle within the Coastal open savanna grasslands in southeastern Kenya. The Mtito Andei-Taita area is situated within the Mozambique Belt, a major structural/metamorphic unit which extends along the African east coast from Mozambique and Malagasy into Sudan and possibly as far north as Egypt and Arabia; it represents one of the fundamental geological features of Africa (Kroner, 1977). The belt consists typically of high-grade metamorphic rocks, characterised by K/Ar-ages of 400-600 MA (Cahen, 1961). Three major units were recognised in southern Kenya: 1) Relics of older metamorphic basement occurring as wedges and slices of charnockites and granulites, tectonically emplaced within meta-sediments; 2) variegated metasediments, consisting of marbles, quartzites, graphite and kyanite (-sillimanite) gneisses and schists; 3) thick suite of monotonous meta-greywackes (quartz-feldspar-biotitehornblende gneisses) with bands of ortho-amphibolites (Pohl and Niedermayr, 1979). Green tourmalines occur in plumasitic pegmatites, plagioclase-mica rocks with ruby and kyanite, which form irregular near-vertical veinlets in the ultramafics and are surrounded by phlogopite-vermiculite-antophyllite alteration zones (Pohl et al., 1980).

The tourmaline sample (hereinafter abbreviated as TAN) originates from Merelani, a world-famous area of gemmological quality minerals, also called the Gemstone Belt of East Africa. Here, gem-quality tourmalines, along with garnets (tsavorite, spessartine and rhodolite), ruby, sapphire, tanzanite, kyanite, diopside and many other minerals were found (Malisa, 2004; Le Goff et al., 2010; Feneyrol et al., 2013; Harris et al., 2014). Merelani area is located in the western part of the Lelatem antiform, approximately 65 km from the city of Arusha in Tanzania (Malisa, 1998, 2004) and consists of granulite complexes of the Pan-African Mozambican zone (Muhongo and Lenoir, 1994). The site extends along the Lelatema fault system, which consists of Proterozoic metasediments, graphitic gneisses, dolomitic marbles and shales. The rocks went through a metamorphic peak from 7.7 to 9.1 kbar and 600-740 °C at 640 Ma, while the Lelatema fracture system formed during deformation at 560 Ma (Muhongo et al., 1999; Hauzenberger et al., 2004, 2007; Malisa, 2004; Le Goff et al., 2010). After the Pan-African tectonothermal event, there was a hydrothermal dissolution of rocks rich in Ca, Mg, CO_2, and SO_3 and also enriched in V, U, Sr, Zn, and HREE. Subsequently, fluids with these elements got into local fractures and fissures, reacting with the bedrock layers. This reaction resulted in the formation of tanzanite and other zoisite varieties, green grossular (tsavorite), diopside, quartz, graphite and calcite (Bocchio et al., 2012).

ANALYTICAL METHODS

Crystal fragments of tourmaline from both localities were selected for the heat treatment. One sample from each locality was heated in the muffle furnace for a total of 24 hours (6 hours heating up to the required temperature, 12 hours on the peak temperature and 6 hours of cooling down) at 700, 800, 900, and 1000 °C in the air atmosphere and atmospheric pressure. The treated samples were labelled according to their locality and the peak temperature as KEN-700, KEN-800, KEN-900, KEN-1000, TAN-700, TAN-800, TAN-900 and TAN-1000.

After the heat treatment, the samples were measured with OAS and then put into polished sections and subjected to EPMA and Raman spectroscopy. Fragments of the samples heated at 1000 °C were ground to powder and measured with PXRD.

The composition of tourmaline and the treatment products was determined by the CAMECA SX100 electron probe micro-analyser (EPMA) at the Masaryk University,

Brno, Czech Republic, operated in wavelength-dispersion mode under the following conditions: accelerating voltage of 15 kV, beam current 20 nA, and beam diameter of 3 to 5 μm. The tourmaline samples were analyzed with following calibrant materials: sanidine (Si*K*α, K*K*α), anatase (Ti*K*α), almandine (Fe*K*α, Al*K*α), chromite (Cr*K*α), $ScVO_4$ (V*K*α), rhodonite (Mn*K*α), forsterite (Mg*K*α), willemite (Zn*K*α), pure Ni_2SiO_4 (Ni*K*α), albite (Na*K*α), wollastonite (Ca*K*α), topaz (F*K*α) and vanadinite (Cl*K*α). The detection limits of the elements measured varied between 0.01 and 0.05 wt%. Raw X-ray intensities were corrected for matrix effects with a zf(rz) algorithm of the X-PHI routine (Merlet, 1994). The theoretical amount of B_2O_3 and H_2O was involved in the calculations.

Powder X-ray diffraction (PXRD) analyses were determined by the BRUKER D8 Advance diffractometer (Department of Mineralogy and Petrology, Comenius University in Bratislava, Faculty of Natural Sciences) under the following conditions: Bragg-Brentano geometry (Theta-2Theta), Cu anticathode (Kα1=1.5406 Å), accelerating voltage 40 kV, beam current 40 mA. Ni Kβ filters were used for stripping Kβ radiation, and data was obtained by the BRUKER LynxEye detector. The step size was 0.01° 2θ, the counting time was 10 s per step, and the range of measurement was 2-65° 2θ. Analysed scans were fitted, and lattice parameters were refined using DIFFRACplus TOPAS software with the structural models of cordierite (Armbruster, 1986) and indialite (Balassone et al., 2004).

Raman analyses were performed on LabRAM-HR Evolution (Horiba Jobin-Yvon) spectrometer system with Peltier cooled CCD detector and Olympus BX-41 microscope (Masaryk University, Department of Geological Sciences). Raman spectra were excited by a 473 nm DPSS laser. A silicon wafer (520.6 cm^{-1}) was used for spectral calibration. Spectra in the range of 50-4000 cm^{-1} for Raman spectra and 50-10,000 cm^{-1} for Raman luminescence spectra were collected using 50 x objective. The acquisition time of 15 s per frame and 2 accumulations were used to improve the signal-to-noise ratio.

The optical absorption spectra of cut stones in the region (500-1000 nm) were measured with the GL Gem Spectrometer™ (Gemlab Group, Vancouver, Canada) with GL Halogen light source (10 W) at room temperature at the Department of Mineralogy, Petrology and Economic Geology, Comenius University in Bratislava.

Raman and UV/Vis/NIR spectra were processed in Seasolve PeakFit 4.1.12 software. Raman and absorption bands were fitted by the Voigt function with variable width, automatic background correction, and Savitsky-Golay smoothing. Band fitting was gradually refined until it produced reproducible results with a square regression coefficient greater than 0.995.

RESULTS

As already mentioned, the studied samples were fragments of crystals of various shapes. Both sets were transparent and green with slightly different hues. The TAN samples have slightly more blue hue than KEN and are closer to the typical emerald green (Figure 1). After the heating, no significant visual changes were observed in TAN samples until the sample breakdown at 1000 °C. In contrast, changes in hue were observed in KEN samples; after the heating at 700 °C, the yellowish tint disappeared, and the colour became striking, almost emerald green. However, when the KEN sample was heated at 900 °C, transparency was suppressed, and the sample became only translucent with a less striking colour. KEN also broke down after heating at 1000 °C.

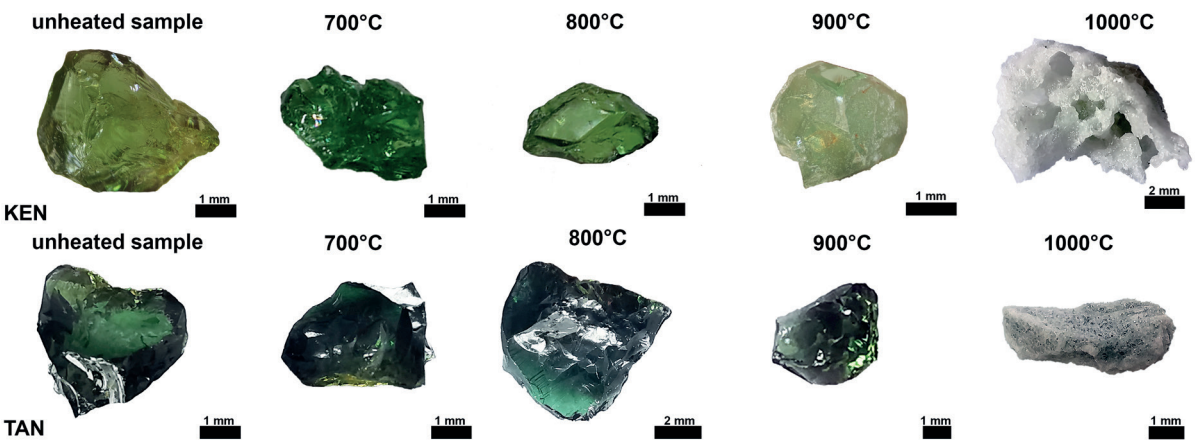

Figure 1. Macroscopic images of studied samples before and after the heat treatment.

The difference in their chemical composition is more significant. Although both are calcic, strongly Mg-dominant and contain Cr and V in various proportions (Tables 1, 2), other differences clearly separate them. The KEN samples can be classified as fluor-uvite, while the classification of TAN is more complicated. It contains magnesio-lucchesiite, magnesio-foitite, and oxy-dravite components in various amounts, but in general, magnesio-

Table 1. Representative chemical compositions of tourmaline from Kenya.

	KEN-700	KEN-700	KEN-800	KEN-800	KEN-900	KEN-900
SiO_2	37.20	37.17	37.90	37.92	38.19	37.99
TiO_2	0.39	0.39	1.06	1.06	0.79	0.84
B_2O_3*	10.95	10.85	10.93	10.98	10.98	10.97
Al_2O_3	29.41	29.09	28.41	28.45	28.96	28.96
Cr_2O_3	0.00	0.02	0.04	0.06	0.02	0.02
V_2O_3	0.20	0.19	0.15	0.15	0.06	0.09
FeO	0.02	0.05	0.00	0.07	0.00	0.05
MnO	0.00	0.00	0.00	0.01	0.00	0.00
MgO	14.87	14.55	14.78	14.94	14.53	14.49
NiO	0.00	0.00	0.00	0.02	0.11	0.09
ZnO	0.00	0.00	0.00	0.00	0.00	0.16
CaO	3.57	3.65	3.65	3.62	3.68	3.44
Na_2O	1.40	1.35	1.39	1.50	1.34	1.43
K_2O	0.06	0.06	0.05	0.05	0.04	0.05
H_2O*	2.88	2.75	2.67	2.73	2.77	2.82
F	1.71	1.69	1.67	1.64	1.42	1.48
Cl	0.01	0.01	0.01	0.02	0.00	0.01
O=F	0.72	0.71	0.70	0.69	0.60	0.62
O=Cl	0.00	0.00	0.00	0.00	0.00	0.00
Total	101.94	101.09	102.01	102.51	102.28	102.28
Si	5.905	5.955	6.024	6.003	6.048	6.019
Al	0.095	0.045	0.000	0.000	0.000	0.000
∑T	6.000	6.000	6.024	6.003	6.048	6.019
B	3.000	3.000	3.000	3.000	3.000	3.000
Ti	0.047	0.047	0.127	0.126	0.094	0.100
Al	5.408	5.447	5.322	5.308	5.405	5.407
Cr	0.000	0.002	0.005	0.007	0.002	0.003
V	0.025	0.024	0.020	0.019	0.007	0.012
Fe^{2+}	0.002	0.006	0.000	0.009	0.000	0.007
Mn	0.000	0.000	0.000	0.001	0.000	0.000
Mg	3.518	3.474	3.502	3.525	3.429	3.423
Zn	0.000	0.000	0.000	0.000	0.000	0.018
Ni	0.000	0.000	0.000	0.003	0.015	0.012
∑Y+Z	9.000	9.000	8.976	8.997	8.952	8.981
Ca	0.607	0.626	0.622	0.614	0.624	0.585
Na	0.431	0.420	0.428	0.460	0.411	0.440
K	0.012	0.013	0.010	0.010	0.009	0.010
$^{X}\square$	0.000	0.000	0.000	0.000	0.000	0.000
∑X	1.050	1.058	1.060	1.085	1.044	1.034
F	0.860	0.856	0.837	0.823	0.710	0.743
Cl	0.002	0.004	0.004	0.004	0.001	0.003
O	0.089	0.205	0.331	0.290	0.365	0.277
OH	3.049	2.936	2.829	2.883	2.925	2.976
∑V+W	4.000	4.000	4.000	4.000	4.000	4.000

Table 2. Representative chemical compositions of tourmaline from Tanzania.

	TAN-700	TAN-700	TAN-800	TAN-800	TAN-900	TAN-900
SiO_2	36.65	36.90	37.25	36.83	37.13	37.08
TiO_2	0.44	0.43	0.42	0.47	0.36	0.36
B_2O_3*	10.67	10.73	10.82	10.75	10.81	10.87
Al_2O_3	32.83	32.86	33.09	32.94	32.94	33.37
Cr_2O_3	0.39	0.31	0.43	0.27	0.69	0.43
V_2O_3	0.08	0.07	0.11	0.11	0.06	0.06
FeO	0.03	0.07	0.01	0.04	0.07	0.02
MnO	0.00	0.00	0.00	0.07	0.05	0.02
MgO	10.73	10.95	10.99	10.98	11.01	11.24
NiO	0.00	0.00	0.00	0.00	0.00	0.00
ZnO	0.00	0.00	0.00	0.00	0.00	0.00
CaO	2.09	2.13	2.25	2.27	2.20	2.29
Na_2O	0.74	1.55	0.74	0.67	0.67	0.70
K_2O	0.06	0.08	0.06	0.06	0.07	0.07
H_2O*	3.32	3.13	3.34	3.37	3.41	3.47
F	0.00	0.00	0.00	0.00	0.00	0.00
Cl	0.00	0.00	0.00	0.01	0.01	0.01
O=F	0.00	0.00	0.00	0.00	0.00	0.00
O=Cl	0.00	0.00	0.00	0.00	0.00	0.00
Total	98.03	99.19	99.51	98.83	99.49	99.98
Si	5.971	5.976	5.984	5.956	5.967	5.926
Al	0.029	0.024	0.016	0.044	0.033	0.074
∑T	6.000	6.000	6.000	6.000	6.000	6.000
B	3.000	3.000	3.000	3.000	3.000	3.000
Ti	0.054	0.053	0.051	0.057	0.043	0.044
Al	6.274	6.247	6.249	6.234	6.207	6.212
Cr	0.050	0.039	0.054	0.035	0.088	0.054
V	0.011	0.009	0.014	0.014	0.008	0.008
Fe^{2+}	0.004	0.009	0.001	0.005	0.009	0.002
Mn	0.000	0.000	0.000	0.009	0.007	0.003
Mg	2.606	2.643	2.632	2.646	2.638	2.678
Zn	0.000	0.000	0.000	0.000	0.000	0.000
Ni	0.000	0.000	0.000	0.000	0.000	0.000
∑Y+Z	9.000	9.000	9.000	9.000	9.000	9.000
Ca	0.365	0.369	0.387	0.393	0.379	0.392
Na	0.234	0.485	0.232	0.210	0.210	0.216
K	0.013	0.016	0.012	0.012	0.015	0.014
$^{X}\square$	0.388	0.129	0.369	0.386	0.397	0.378
∑X	0.612	0.871	0.631	0.614	0.603	0.622
F	0.000	0.000	0.000	0.000	0.000	0.000
Cl	0.001	0.000	0.000	0.003	0.001	0.001
O	0.392	0.616	0.419	0.360	0.338	0.301
OH	3.607	3.384	3.581	3.637	3.661	3.697
∑V+W	4.000	4.000	4.000	4.000	4.000	4.000

lucchesiite prevails.

Other differences are apparent when details are considered. KEN has almost no *X*-site vacancies, while in TAN, the proportion of *X*-site vacancies to Ca is approximately 1:1, and Na is minor (Figure 2a). When the W occupancy is considered, KEN is F-dominant with minor O and negligible OH. In contrast, the TAN sample is very poor in F and belongs to the hydroxy-tourmaline series with significant O content (Figure 2b). Based on the Ca/(Ca+Na) and Al proportion, KEN can be classified as fluor-uvite, while TAN is in the field of magnesio-lucchesiite (Figure 2c). There is a clear difference between the samples in the V and Cr proportion (Figure 2d). The V content is relatively similar in both samples (0.005-0.025 apfu), although KEN is slightly richer in V. In contrast, Cr content is below 0.007 apfu in KEN but is distinctly higher in TAN, varying between 0.03 and 0.09 apfu.

The Raman spectra of both sets of samples with bands assigned to A_1 and E modes and various types of vibrations (Table 3) show some similarities and also some differences (Figure 3). The most intensive vibrations in all samples are at 369-375 and 709-725 cm^{-1}. The occurrence of bands and actual intensity depended on the orientation of the sample, which was random and different in each sample. Therefore, we do not emphasise it. However, the position of bands could indicate subtle crystal-chemical differences between samples. The position of bands below 250 cm^{-1}, which are assigned to the stretching of Mg-O, V-O and Cr-O, could depend on the variable content of specified cations. These variations can also be

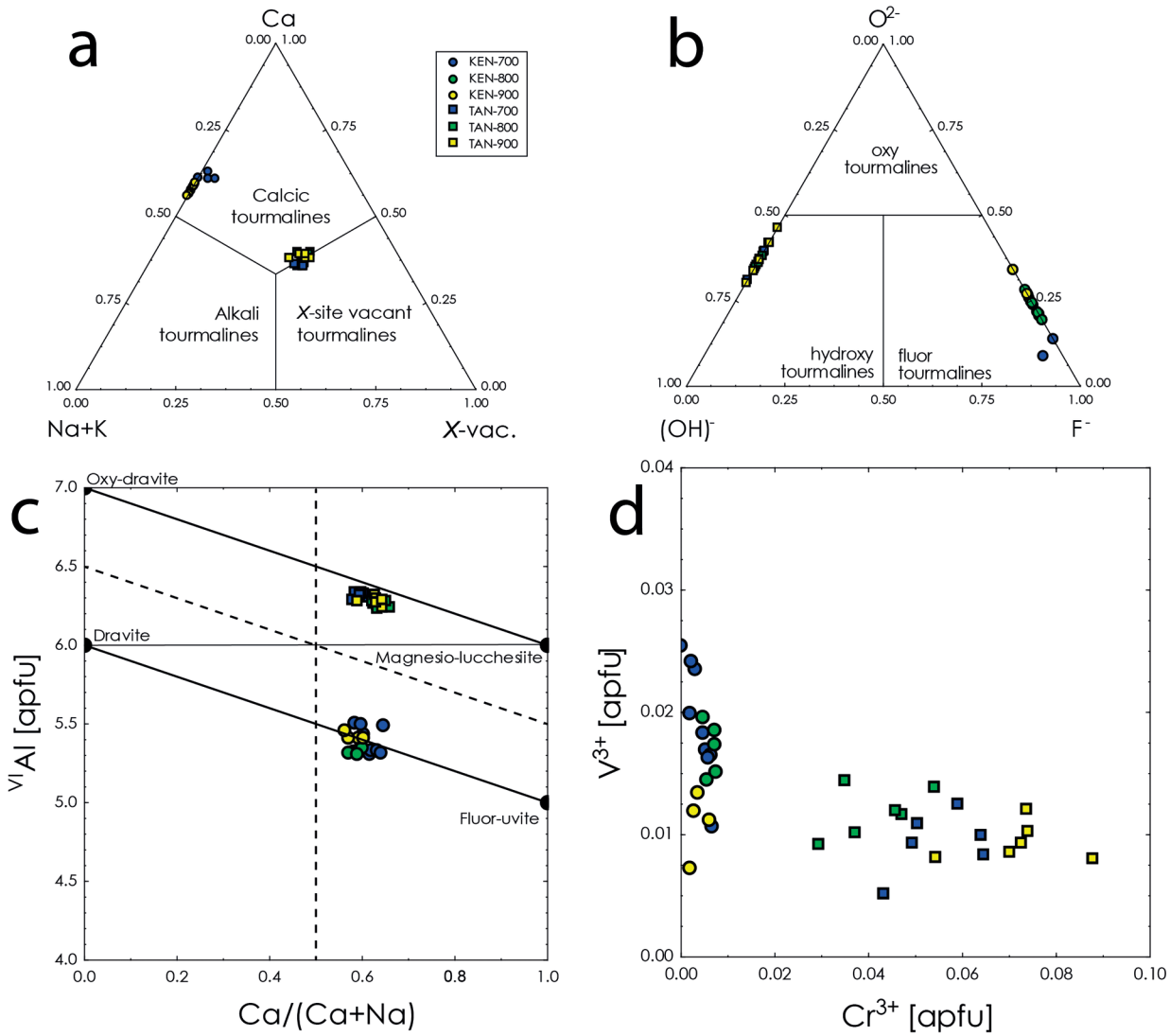

Figure 2. The chemical composition and classification of studied samples.

Table 3. Position of bands in Raman spectra of studied samples. The Raman bands were assigned to various types of modes according to Gasharova et al. (1997) for the region between 100-1200 cm^{-1} and according to Berryman et al. (2016) for OH vibrations.

		KEN-700	KEN-800	KEN-900	TAN-700	TAN-800	TAN-900
Mg-O, V-O, Cr-O stretching	A_1	214	210	210	213	217	218
Mg-O, V-O, Cr-O stretching	A_1	243	241	241	248	232	227
O-Al-O bending	E	275	273	271			
Si-O_{non} rocking	A_1, E	342	345	340	341	339	340
Al-O stretching	A_1	375	370	369	369	371	369
O_{non}-Si-O_{non} bend	A_1, E				530	539	527
Si-O_{br} rocking	A_1	630	629	634			
Si-O_{br} rocking	A_1	668	667	668	660	660	660
B-O stretching & B-O-Al bend	E		704	707			
"breathing" of O_{br} in Si-O rings	A_1	725			722	725	720
Si-O stretching & Si-O-Si bending	A_1	761	759	757	781	769	770
B-O-Al bending	A_1	818	817	817			
Si-O stretching			975	969		966	971
Si-O_{non} stretching		1045	1035	1044			
Si-O_{non} stretching			1064	1065	1066	1065	1068
Si-O_{br} stretching		1074					
^{V}OH		3587	3583	3579	3567	3573	3571
^{W}OH		3627	3627	3628			

the cause of a shift of O-H bands. In the TAN samples, the band assigned to ^{V}(OH) is centred at 3567-3571 cm^{-1}, while this band is split and shifted to 3579-3587 cm^{-1} with a shoulder at 3598-3601 cm^{-1}. Moreover, KEN samples display a weak band at 3627-3628 assigned to ^{W}(OH).

Very intensive luminescence was observed in the Raman spectra of all samples. Therefore, the Raman luminescence spectra were measured up to 10,000 cm^{-1}. The conversion to wavelength revealed that the sharp intensive band is located at 680-684 nm (Table 4) accompanied by the broad band between 690 and 900 nm (Figure 4).

All studied samples are green and contain variable proportions of Cr and V. Therefore, their OAS spectra look similar, with two major absorption bands in blue and yellow to red regions (Figure 5). The spectra of samples also did not significantly change after heating up to 900°C. However, after the fitting of absorption bands, several minor differences are observed (Table 5). Firstly, in the OAS spectrum of the original KEN sample, there is an additional band at 742 nm, which disappeared in the heated samples (Figure 5). There are also slight shifts of main bands, which do not seem to be systematic. Moreover, after the heating at 800 and 900 °C, there is a change in absorbance, which, although it cannot be quantified from the measured data, can indicate a decrease in the transparency of samples.

The spectra of TAN samples also differ from those of KEN (Figure 5, Table 5). The 604-608 nm absorption band has a shoulder band located at 692-694 nm. Moreover, the band in the blue region is asymmetrical, and its fitting revealed that it is split into bands centred at 402-408 and 449-456 nm.

As mentioned above, the KEN sample showed signs of breakdown on the rim already at 900 °C. The narrow rim was likely composed mostly of glass, but crystals of cordierite/indialite and small crystals (up to 30 μm) of unknown phase (composition in wt% of oxides 29.58 SiO_2, 1.25 TiO_2, 23.18 Al_2O_3, 0.20 V_2O_3, 0.02 Cr_2O_3, 0.04 MnO, 15.20 MgO, 0.04 BaO, 0.25 SrO, 6.80 CaO, 1.46 Na_2O, 0.04 K_2O, 0.24 F) were found. However, Raman spectroscopy did not provide a sufficiently resolvable spectrum.

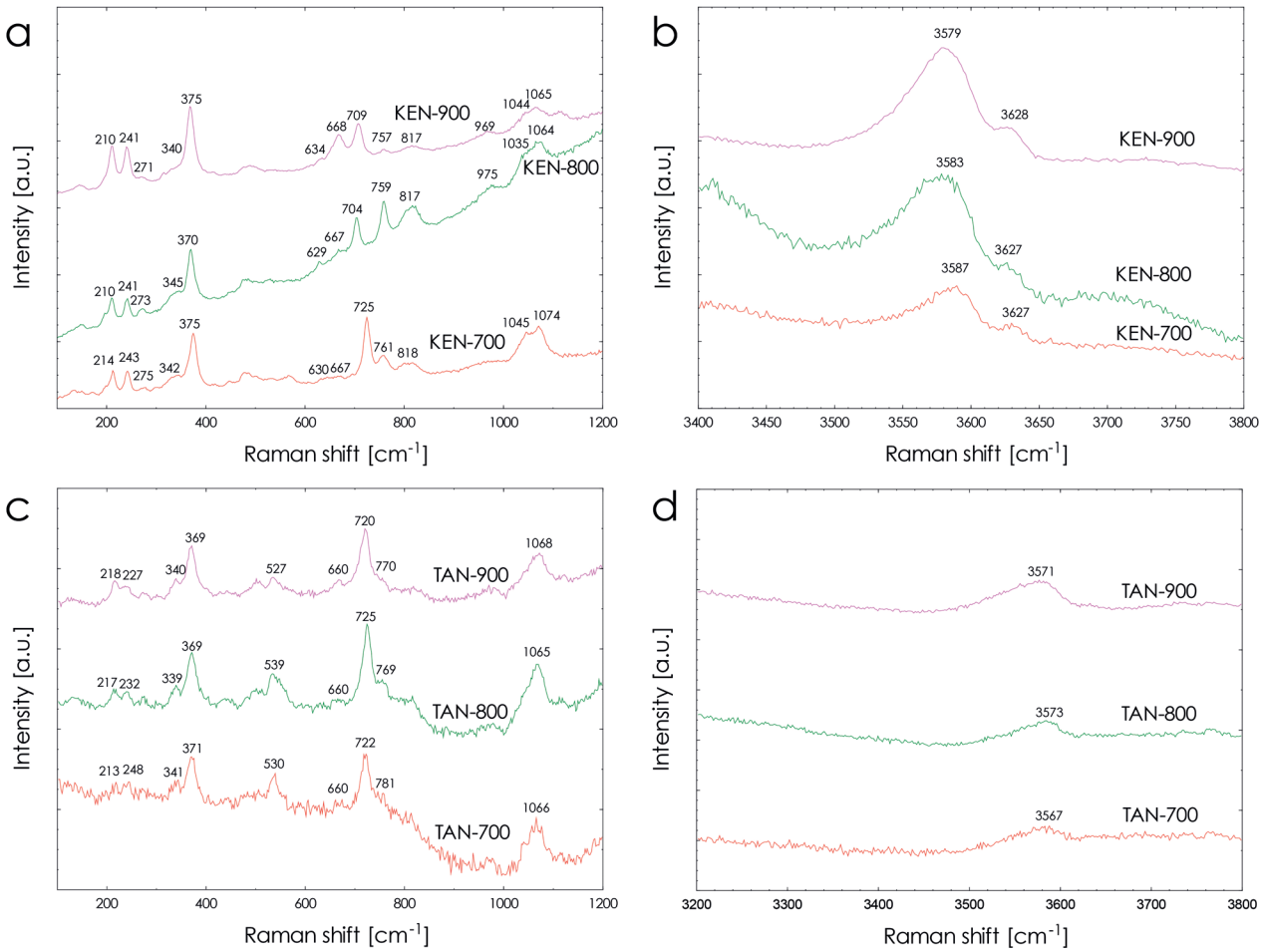

Figure 3. The Raman spectra of studied samples.

Table 4. Position of the prominent luminescence band in the Raman luminescence spectrum.

Centre	Transition	KEN-700		KEN-800		KEN-900	
		nm	cm^{-1}	nm	cm^{-1}	nm	cm^{-1}
Cr^{3+}	$^4A_{2g}\rightarrow{}^4T_{1g}$	680	14.716	680	14.710	680	14.709
		683	14.640	683	14.640	683	14.646
		TAN-700		TAN-800		TAN-900	
Cr^{3+}	$^4A_{2g}\rightarrow{}^4T_{1g}$	684	14.620	684	14.620	684	14.620

After the heating at 1000 °C, both samples visually changed completely. Both lost their original green colour and turned white to greyish white. Moreover, they expanded and became porous (Figure 1). However, there is a difference in the extent of the expansion and the size of pores between the two samples; the KEN sample had expanded much more than the TAN sample.

The breakdown products were identified by EPMA and PXRD (Figures 6, 7, Tables 6-8). An amorphous glass phase was present in both samples. Moreover, the remnant of the original tourmaline was still present in the core of the TAN sample. The difference between samples was in the number of crystalline phases that were the breakdown products. The KEN sample breakdown produced only the

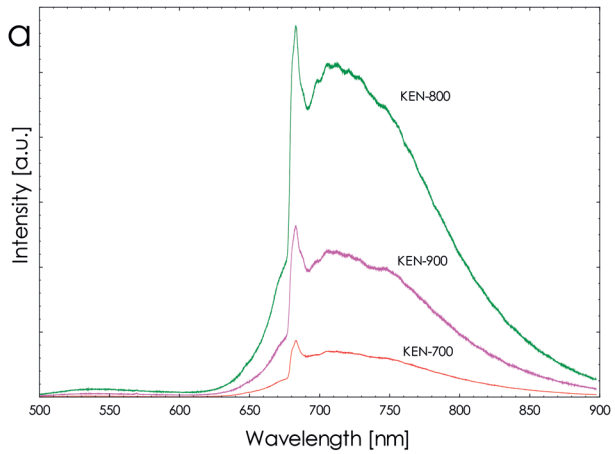

Figure 4. The Raman luminescence spectra of studied samples.

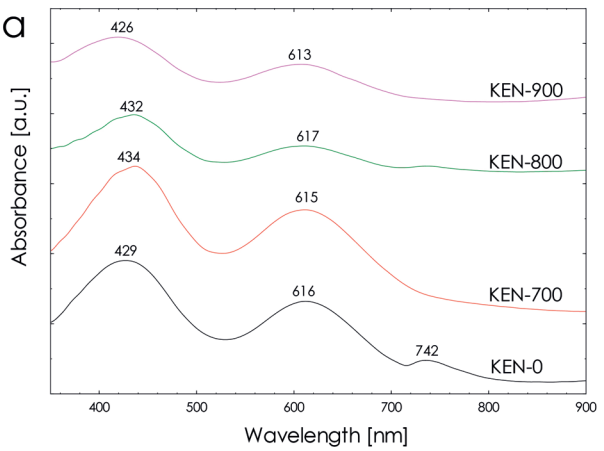

Figure 5. The optical absorption spectra of studied samples.

Table 5. Position of bands in the optical absorption spectra of studied samples.

Centre	Transition	KEN-0		KEN-700		KEN-800		KEN-900	
		nm	cm^{-1}	nm	cm^{-1}	nm	cm^{-1}	nm	cm^{-1}
V^{3+}	$^3T_{1g} \rightarrow {}^3T_{1g}$	429	23.310	434	23.041	432	23.310	426	23.474
V^{3+}	$^3T_{1g} \rightarrow {}^3T_{2g}$	616	16.234	615	16.260	617	16.207	613	16.313
CFT $^{Y}Fe^{2+}$-$^{Y,Z}Fe^{3+}$	$^5T_{2g} \rightarrow {}^5E_g$	742	13.477						
		TAN-0		TAN-700		TAN-800		TAN-900	
Cr^{3+}	$^4A_{2g} \rightarrow {}^4T_{1g}$	402	24.876	405	24.691	405	24.691	408	24.510
Cr^{3+}	$^4A_{2g} \rightarrow {}^4T_{1g}$	452	22.124	456	21.930	456	21.930	449	22.272
Cr^{3+}	$^4A_{2g} \rightarrow {}^4T_{2g}$	604	16.556	605	16.529	608	16.447	604	16.556
Cr^{3+}	$^4A_{2g} \rightarrow {}^2T_{1g}$	694	14.409	692	14.451	693	14.430	693	14.430

phase with the cordierite or indialite structure, which was slightly depleted in Si and enriched in Al, Mg and channel alkali Ca and Na (Table 6).

In contrast, TAN broke down into more crystalline phases, including cordierite/indialite, a mullite-like phase and spinel (Figure 6, 7, Tables 6-8). Cordierite/indialite forms prismatic and skeletal crystals (Figure 6 b,d), mullite-like phase crystals are prolonged, thin-

Table 6. Representative chemical compositions of breakdown products.

	KEN-1000	KEN-1000	TAN-1000	TAN-1000
	glass	Crd	Crd	Mul?
P_2O_5	0.00	0.00	0.04	0.00
SiO_2	37.75	49.20	52.05	22.49
TiO_2	0.83	0.31	0.14	0.58
Al_2O_3	28.85	36.25	33.09	46.53
V_2O_3	0.09	0.00	0.00	0.05
Cr_2O_3	0.05	0.01	0.05	2.96
FeO	0.00	0.01	0.00	0.02
MnO	0.02	0.02	0.01	0.00
MgO	14.62	14.15	13.90	24.14
ZnO	0.09	0.02	0.07	0.16
NiO	0.00	0.18	0.03	0.00
BaO	0.04	0.00	0.00	0.01
SrO	0.06	0.00	0.01	0.17
CaO	3.58	0.33	0.17	0.55
Na_2O	1.35	1.26	0.42	0.16
K_2O	0.04	0.09	0.03	0.01
F	1.45	0.07	0.02	0.04
Cl	0.03	0.00	0.00	0.00
Total	88.84	101.90	100.04	97.88
P^{5+}		0.000	0.003	0.000
Si^{4+}		4.771	5.111	1.150
Ti^{4+}		0.023	0.010	0.022
Al^{3+}		4.143	3.829	2.805
V^{3+}		0.000	0.000	0.002
Cr^{3+}		0.000	0.004	0.120
Fe^{2+}		0.001	0.000	0.001
Mn^{2+}		0.002	0.000	0.000
Mg^{2+}		2.045	2.034	1.841
Zn^{2+}		0.001	0.005	0.006
Ni^{2+}		0.014	0.003	0.000
Sr^{2+}		0.000	0.001	0.005
Ca^{2+}		0.035	0.018	0.030
Na^{+}		0.237	0.081	0.016
K^{+}		0.011	0.004	0.001
Cations		11.000	11.000	6.000
F^{-}		0.022	0.006	0.007
Cl^{-}		0.000	0.000	0.000

prismatic to acicular (Figure 6c), and spinel is euhedral (Figure 6d). Cordierite/indialite in this sample is closer to end-member composition with slightly increased Si and a lower proportion of channel alkali (Table 6). The composition of the mullite-like phase is quite different to the stoichiometric end-member composition, but the EPMA analyses did not include B, which can be present in its structure (Table 6). Spinel is close to the end member composition except for the Cr enrichment (Table 7). The variations in the Cr content are responsible for the zoning observed in the BSE image (Figure 6d).

DISCUSSION

The results of various and complexly used analytical methods connected with visual observation show that during heating, no structural, crystal-chemical, or optical properties significantly changed at temperatures up to 800°C for the KEN sample and 900 °C for the TAN sample. In the rim of the KEN sample heated at 900 °C, a very thin layer of breakdown products obscuring the transparency of the crystal occurred. At 1000 °C, both samples broke down. The structural stability of crystals was evidenced by the Raman spectra, which showed no significant changes. Even bands of OH vibrations stayed intact until the structural breakdown at 1000 °C, indicating the absence of a deprotonation process disregarding oxidation of Fe and Mn, which are present in minute amounts (below 0.1 wt% of oxide).

Colour changes and possible oxidation processes were studied with optical absorption spectroscopy. Spectra of all samples with two main absorption bands in the visible-light range are typical for minerals where V and Cr are the main chromophores. Since both elements are present in all samples, the resulting absorption bands are composites of Cr and V absorption. However, the Cr/V ratio influenced the position of the bands as it is well visible on the ca. 610 nm band (Figure 8). In the Cr-richer TAN sample, the bands shift inversely proportionally with the increasing Cr/V from 608 to 604 nm. In contrast, KEN has low Cr/V (below 1), and the band is located between 613-617 nm. Moreover, there are small variations in individual samples in each set.

The variations in absorption band position result in different colour hues. The transmission area in the green visible light region is between 530-520 nm for the KEN samples and 520-515 nm for TAN, which is why the colour of the KEN sample is more yellowish than that of TAN (Table 9). Moreover, the transmission centres are shifted towards smaller wavelengths after heating both samples, resulting in a more attractive emerald-green colour.

Relatively well-defined optical absorption bands allowed the crystal-field calculations for V^{3+} in KEN and Cr^{3+} in the TAN sample (Table 10). We must consider that both

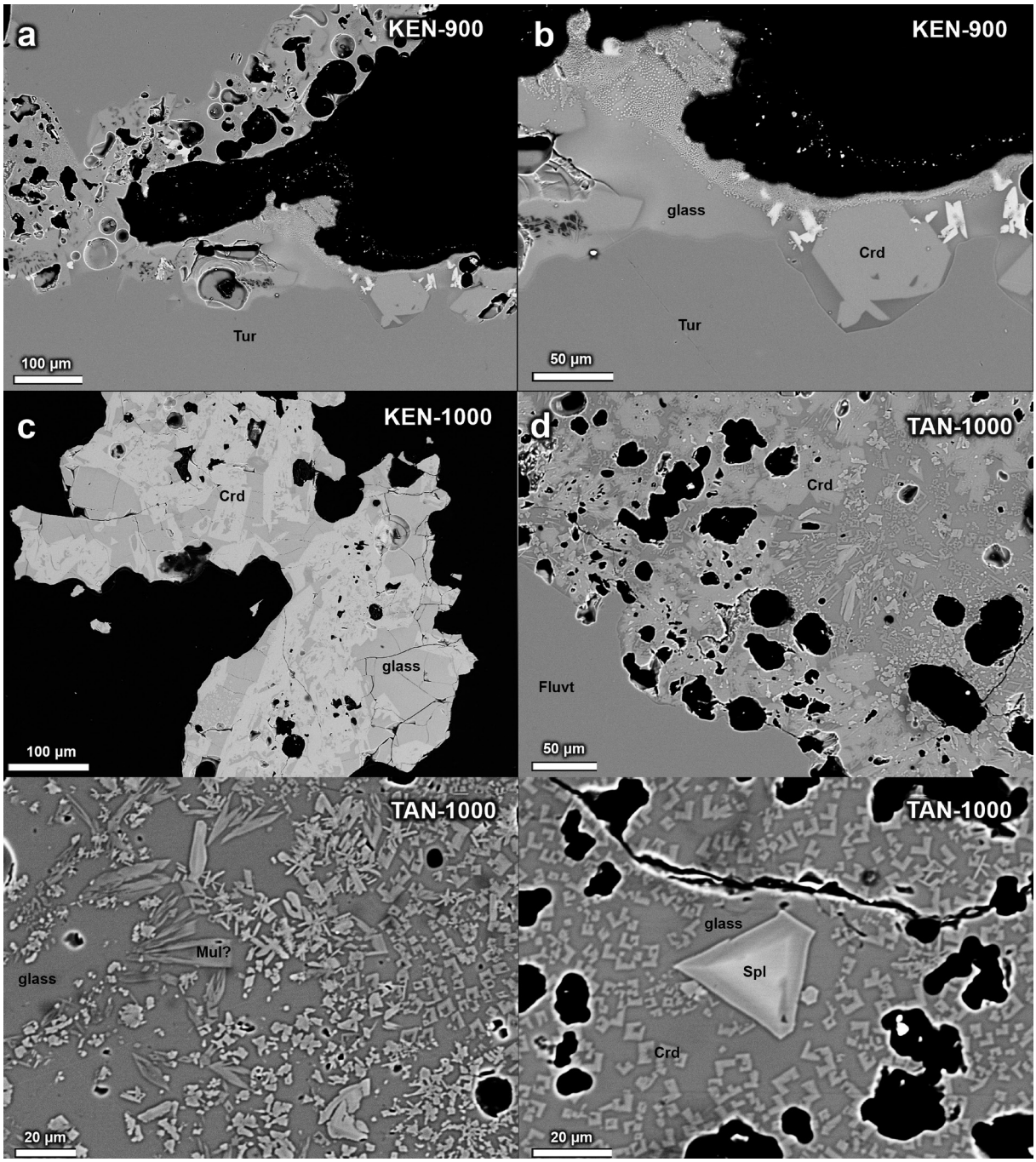

Figure 6.The backscattered electron images of studied samples after their structural breakdown.

sets of samples contain both elements, but in each sample, one is relatively clearly dominant compared to the second one. Therefore, the effects of Cr^{3+} in KEN and V^{3+} in TAN are minor. The calculations revealed crystal field crystal-field splitting energy Δ_{oct} of 17,428 cm^{-1} for V^{3+} in the KEN sample and 16,556 cm^{-1} for Cr^{3+} in the TAN sample. This difference may result from different bond strengths in the octahedra of both samples. The KEN sample contains more Mg than TAN. Therefore, it is more probable that the VO_6 octahedron shares edges with MgO_6 octahedra in this sample, which results in slightly stronger and shorter V-O bonds than in the case of neighbouring AlO_6 octahedra. This, in return, produces a slightly stronger crystal field on V^{3+} compared to Cr^{3+} in the TAN sample.

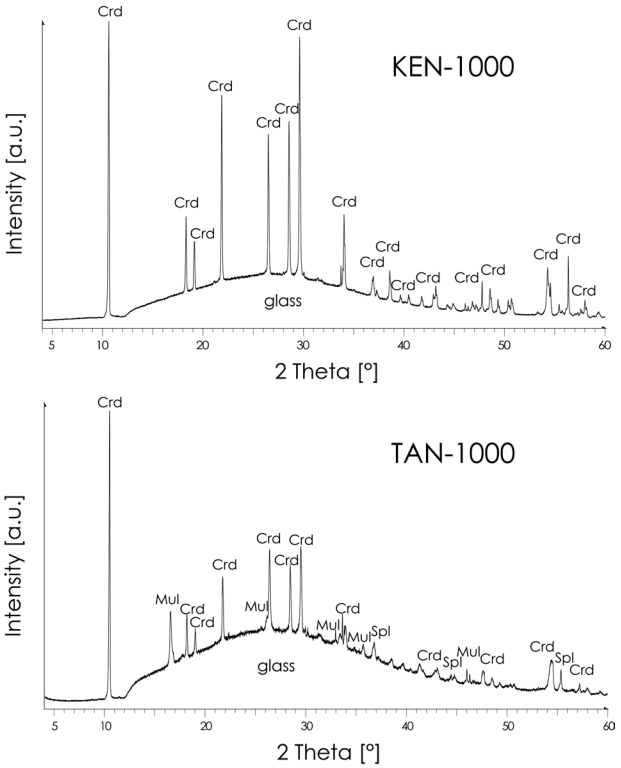

Figure 7. The powder XRD patterns of studied samples after their structural breakdown.

Table 7. Representative chemical compositions of spinel as a breakdown product in TUV sample.

	TUV1000	TUV1000	TUV1000	TUV1000
TiO_2	0.02	0.04	0.03	0.03
Al_2O_3	66.08	66.68	62.59	68.03
V_2O_3	0.18	0.20	0.18	0.22
Cr_2O_3	5.03	4.25	8.44	3.21
Fe_2O_3	0.04	0.05	0.03	0.06
MnO	0.00	0.02	0.02	0.01
MgO	27.96	28.23	27.36	27.85
ZnO	0.04	0.00	0.05	0.02
NiO	0.01	0.00	0.02	0.08
CoO	0.02	0.00	0.02	0.02
CaO	0.04	0.03	0.02	0.07
suma	99.40	99.48	98.76	99.58
Al^{3+}	1.887	1.897	1.821	1.930
V^{3+}	0.003	0.004	0.004	0.004
Cr^{3+}	0.096	0.081	0.165	0.061
Fe^{3+}	0.001	0.001	0.001	0.001
Ti^{4+}	0.000	0.000	0.000	0.000
Mg^{2+}	0.013	0.017	0.010	0.004
B	2.000	2.000	2.000	2.000
Mn^{2+}	0.000	0.000	0.000	0.000
Mg^{2+}	0.997	0.999	0.997	0.995
Zn^{2+}	0.001	0.000	0.001	0.000
Ni^{2+}	0.000	0.000	0.000	0.001
Co^{2+}	0.000	0.000	0.000	0.000
Ca^{2+}	0.001	0.001	0.001	0.002
A	1.000	1.000	1.000	1.000

There is an additional band in the optical spectrum of the original KEN sample at 742 nm (13,477 cm^{-1}), which can be attributed to electronic transitions of Fe^{2+} (Mattson and Rossman, 1984, 1987). This band does not occur in the heated samples, which suggests oxidation of Fe. Electronic transitions in Fe^{3+} generally produce three sets of bands in the visible and near-infrared. Two of these are broad bands in the regions of 750-1,000 nm and 550-700 nm, and the most distinctive sharp band is in the region 410-450 nm (Mattson and Rossman, 1984, 1987). However, 410-450 nm and 550-700 nm regions coincide with the V and Cr absorption, which very likely disguised any possible Fe^{3+} absorption. The band in the 750-1,000 nm should not coincide with any absorption from main chromophores, but it is usually very broad and strongly dependent on the orientation of the sample (Mattson and Rossman, 1984, 1987). Therefore, the measurement of the studied samples with unspecific orientation could not detect this feature. However, the oxidation of Fe during heating at T>700 °C is a well-established phenomenon (Bačík et al., 2011; Ertl et al., 2012; Filip et al., 2012). This Fe oxidation could contribute to the enhancement of tourmaline colour.

Moreover, indirect evidence of the Fe oxidation in the KEN sample was provided by the Raman luminescence spectroscopy. Chromium is a strong luminophore in the range of 650-850 nm. In contrast, Fe^{2+} is among the most important quenchers in minerals, with intense charge-transfer bands in the red to NIR region (Gaft et al., 2005). However, Fe^{3+} has only low absorbance in 650-850 nm, and the most intensive absorption is in the UV to blue-light region (Mattson and Rossman, 1984, 1987). Consequently, Fe loses strong quenching properties after the oxidation from a divalent to a trivalent state. This can explain the difference between the luminescence intensity of samples heated at 700 and 900 °C. The KEN-700 and -900 samples have very similar proportions of Cr and

Fe (KEN-800 has slightly higher Cr content), but the luminescence of KEN-900 has an intensity of more than twice as big. This may result from incomplete oxidation of Fe at 700 °C; therefore, a part of unoxidised Fe^{2+} still could work as a quencher, while fully oxidised Fe at 800 and 900 °C lost this ability.

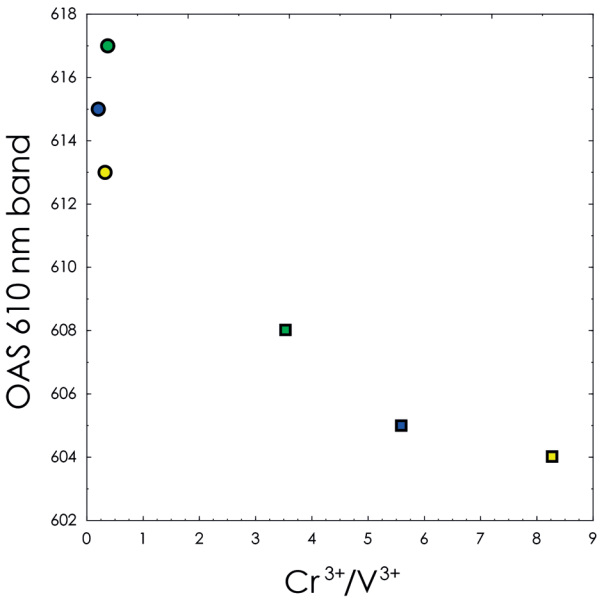

Figure 8. The correlation of the Cr^{3+}/V^{3+} ratio vs optical absorption band located around 610 nm in studied samples.

The samples also showed similarities and differences after their breakdown. The KEN sample started to break down even at 900 °C from the rim, while the TAN sample displayed no signs of decomposition. After the heating at 1000 °C, both samples broke down with very similar effects. Both of them changed to white and increased in volume with the development of pores. This expansion suggests that the fluid phase was not released continuously during heating due to the oxidation of transitional elements such as Fe or Mn, and water was released suddenly after the structural breakdown (Kardošová et al., 2024). However, the KEN sample expanded more with larger pores than TAN (Figure 6). This might result from a slightly higher proportion of volatile elements in the KEN sample (Table 1) if we assume both OH and F were released after the breakdown. On the other hand, the TAN sample is slightly enriched in oxy-tourmaline components (Table 2).

The role of specific elements in the structural stability of samples is questionable. For example, F in the structure of silicates usually increases their high-T stability, as in phlogopite (Sun et al., 2022; Steenstra et al., 2024). However, the KEN sample with fluor-uvite composition had already started to break down at 900 °C. In contrast, the TAN sample was not completely transformed into new products even at 1000 °C; the original tourmaline remained in the core. Consequently, the role of fluorine in stabilising the structure was negligible. This may

Table 8. Unit-cell parameters of cordierite/indialite as the breakdown product in the studied sample refined with structural models of cordierite (Armbruster, 1986) and indialite (Balassone et al., 2004).

		a	***b***	***c***	***V***	R Bragg
		Å	Å	Å	$Å^3$	
KEN1000	cordierite	16.948(2)	9.745(1)	9.339(1)	1542.4(3)	21.59
	indialite	9.776(1)		9.350(2)	773.8(2)	36.32
TAN1000	cordierite	16.926(2)	9.713(3)	9.330(2)	1533.9(5)	12.62
	indialite	9.763(3)		9.317(3)	769.1(5)	26.93

Table 9. Centres of transmission areas in the optical absorption spectra of studied samples.

Centre	KEN-0		KEN-700		KEN-800		KEN-900	
	nm	cm^{-1}	nm	cm^{-1}	nm	cm^{-1}	nm	cm^{-1}
Transmission	529	18.904	524	19.084	524	19.084	521	19.194
	TAN-0		TAN-700		TAN-800		TAN-900	
Transmission	520	19.231	519	19.268	518	19.305	516	19.380

Table 10. Crystal-field parameters and calculated and empirical position of bands for electronic transitions in V^{3+} and Cr^{3+}.

			Δ/B	E/B					B	Δ_{oct}	Position of bands [cm^{-1}]				Position of bands [nm]			
				$^3T_{2g}$	$^3T_{1g}$	$^3A_{2g}$	^2E_g	$^4T_{1g}/^4T_{2g}$			$^3T_{2g}$	$^3T_{1g}$	$^3A_{2g}$	^2E_g	$^3T_{2g}$	$^3T_{1g}$	$^3A_{2g}$	^2E_g
KEN	V^{3+}	calc.	32	29	42	61	17	1.436	552	17428	16234	23311	33662	9617	616	429	297	1040
		emp.									16234	23310			616	429		
				$^4T_{2g}$	$^4T_{1g}$	$^2T_{1g}$	^2E_g	$^4T_{1g}/^4T_{2G}$	B	Δ_{oct}	$^4T_{2g}$	$^4T_{1g}$	$^2T_{1g}$	^2E_g	$^4T_{2g}$	$^4T_{1g}$	$^2T_{1g}$	^2E_g
TAN	Cr^{3+}	calc.	25	25	35	22	21	1.419	674	16556	16556	23500	14603	14171	604	426	685	706
		emp.									16556	24876[a]	14409[c]		604	402[a]	694[c]	
												22124[a]	14620[d]			452[a]	684[d]	
												23500[b]				427[b]		

Notes: a – observed split band in the optical spectrum; b – average position of the split band; c – observed band shoulder of forbidden electronic transition in the optical spectrum; d – luminescence band in Raman luminescence spectrum.

result from the different positions and crystal-chemical processes stabilising phlogopite structure. In micas, F increases the strength of hydrogen bonds between the layers because its electronegativity is higher than O (Sun et al., 2022). However, fluorine in tourmaline is at the O1 site and forms no hydrogen bonds because the orientation of ^{V}OH is completely different, forming hydrogen bonds with the O5 site (Hawthorne, 2002). This process cannot play a role in increasing tourmaline structural stability.

The main factor for different structural stability of fluor-uvite and magnesio-lucchesiite can be found in their octahedral-sites occupancy and Al/Mg ratio. The 3D network of the ZO_6 octahedra is the most important building block of the tourmaline structure, containing the structural islands of tetrahedral rings and YO_6 triplets (Bosi, 2018). Consequently, it is expected that the *Z*-site occupancy has a strong impact on structural stability. Moreover, the *Y*-site occupancy can also be considered because if we assume the occupancy is similar to other sites, the difference here can also play a role in the breakdown process. Magnesio-lucchesiite in TAN samples contains more than 6.2 apfu Al, while below 5.5 apfu in fluor-uvite in the KEN sample. This means that a significant part of Mg is located at the Z site of fluor-uvite due to uvite substitution (Henry and Dutrow, 1990). However, in magnesio-lucchesiite, if any Mg is at the Z site, it is only due to Mg-Al disorder (Hawthorne et al., 1993). Although we have no structural analysis of the studied samples, comparison with the other magnesio-lucchesiite occurrences suggests that Mg-Al disorder is insignificant in this composition (Scribner et al., 2021; Sęk et al., 2023).

This can have a significant influence on the stability of the structure. In the uvite structural arrangement, the calculated bond valence sum (BVS) is 2.87 vu (valence units) for the Z site and 1.97 vu for Y, while it is 3.05 vu for Z and 2.31 vu for the Y site in oxy-dravite (Bačík, 2024). Although the structural arrangements for fluor-uvite and magnesio-lucchesiite are slightly different to those in uvite and oxy-dravite, respectively, they are sufficiently similar. Therefore, we can assume that stronger bonds at both the Z and Y sites of magnesio-lucchesiite make the structure stable in the higher T conditions compared to fluor-uvite.

The breakdown products also slightly differ between samples. The KEN sample heated at 1000 °C contained only cordierite/indialite and glass, although the unknown silicate phase occurred in the rim of the sample heated at 900 °C. The ratio of main oxides does not correspond to any known mineral phase, but it is closest to ardennite-group minerals. The formula calculated based on 16 cations of $Ca_{1.280}Na_{0.498}Sr_{0.026}K_{0.008}Ba_{0.003}Al_{4.802}Mg_{3.984}Ti_{0.165}V_{0.028}Mn_{0.006}Cr_{0.002}Si_{5.199}O_{22}(OH,F)_6$ show similarity to the hypothetical Mg- and Al-dominant analogue of ardenite-(V), but there is not sufficient analytical evidence for this claim.

In contrast, the breakdown of the TAN sample led to a more diverse association of cordierite/indialite, mullite-like phase and spinel. Indialite is a polymorph of cordierite with topologically identical structure differing only in ordering at tetrahedral sites, which induces a reduction in symmetry of the tetrahedral ring and, consequently, a reduction in the whole-structure symmetry (Miyashiro and Iiyama, 1954; Miyashiro et al., 1955; Armbruster and Bloss, 1981; Armbruster, 1985). Indialite is a stable phase for high-temperature and low-pressure metamorphic environments (Schreyer et al., 1990; Balassone et al., 2004). Therefore, based on the high-temperature

conditions, indialite is a more likely phase than cordierite. However, the refinement of the PXRD pattern (Table 8) using the cordierite structural model (Armbruster, 1986) produced a lower R than one with the indialite structure (Balassone et al., 2004). This might indicate that there can be an extensive ordering of Al and Si present during the cooling of the sample, which could be allowed to the very small size of cordierite/indialite crystals.

The mineral association in the TAN-1000 sample is similar to the breakdown products of uvite from San Piero in Campo, Elba, Italy, which included indialite, yuanfuliite, plagioclase, a "boronmullite" phase, and hematite (Ballirano et al., 2022b). The difference can be attributed to several factors. The absence of hematite in our samples is clearly connected with the extremely low Fe content in the TAN sample, up to 0.01 apfu compared to 0.47 apfu Fe^{2+} and 0.32 apfu Fe^{3+} in uvite from San Piero in Campo (Bosi et al., 2022). The presence of borosilicate phases is questionable. We assume that part of B can be stored in the mineral with the structure of mullite, which is evident in the TAN sample. However, no other borosilicate phases, including yuanfuliite, were sufficiently demonstrable in the EPMA, Raman spectra or PXRD pattern.

CONCLUSIONS

The experimental high-temperature, low-pressure research of tourmalines with various compositions still brings new and interesting data. Two tourmalines with many common features, such as the dominance of Ca at the *X* site, extremely high ^{X}Mg and low Fe content, and significant Cr and V content resulting in the green colour, but a few differences, including Al vs Mg content, Cr/V ratio, the W occupancy and overall mineral classification (fluor-uvite vs magnesio-lucchesiite to magnesio-foitite), showed similar behaviour in some ways and different behaviour in other ways. Both sets of samples showed structural stability, including only negligible to unobservable oxidation and deprotonation effects after heating up to 800 °C. There were slight differences in samples heated at 900 °C; magnesio-lucchesiite in the KEN sample showed signs of structural breakdown on the rim, while fluor-uvite in TAN remained intact. After heating at 1000 °C, both samples broke down with slightly different associations of breakdown products: cordierite/indialite and glass from magnesio-lucchesiite, and cordierite/indialite, mullite-like phase, spinel and glass from fluor-uvite. Moreover, in the core of the TAN sample, the remnant of fluor-uvite stayed intact. There was also a volumetrical difference between the samples after the breakdown; both samples expanded in volume, but the KEN sample expanded more with larger pores. This likely resulted from a higher proportion of volatile phase in this sample.

ACKNOWLEDGEMENTS

The authors are indebted to Alessandro Pacella for editorial handling and anonymous reviewer for their detailed reviews and very useful suggestions. The Slovak Research and Development Agency supported this work under contract No. APVV-18-0065, and projects VEGA-1/0137/20 and VEGA-1/0189/23.

REFERENCES

Armbruster T., 1985. Crystal structure refinement, Si,Al-ordering, and twinning in "pseudo-hexagonal" Mg-cordierite. Neues Jahrbuch fur Mineralogie, Monatshefte H6, 255-267.

Armbruster T., 1986. No role of Na in the structure of low-cordierite; a single-crystal X-ray study. American Mineralogist 71, 746-757.

Armbruster T. and Bloss F.D., 1981. Mg-cordierite: Si/Al ordering, optical properties, and distortion. Contributions to Mineralogy and Petrology 77, 332-336.

Bačík P., 2024. The bond-topological field modelling I: The bond-topological map of dravite from Forshammar, Sweden. In press.

Bačík P., Ozdín D., Miglierini M., Kardošová P., Pentrák M., Haloda J., 2011. Crystallochemical effects of heat treatment on Fe-dominant tourmalines from Dolní Bory (Czech Republic) and Vlachovo (Slovakia). Physics and Chemistry of Minerals 38, 599-611.

Balassone G., Franco E., Mattia C.A., Puliti R., 2004. Indialite in xenolithic rocks from Somma-Vesuvius Volcano (southern Italy): crystal chemistry and petrogenetic features. American Mineralogist 89, 1-6.

Ballirano P., Celata B., Skogby H., Andreozzi G.B., Bosi F., 2022a. HT breakdown of Mn-bearing elbaite from the Anjanabonoina pegmatite, Madagascar. Journal of Geosciences 67, 151-161.

Ballirano P., Celata B., Bosi F., 2022b. In situ high-temperature behaviour and breakdown conditions of uvite at room pressure. Physics and Chemistry of Minerals 49, 1-10.

Berryman E.J., Wunder B., Rhede D., Schettler G., Franz G., Heinrich W., 2016. P-T-X controls on Ca and Na distribution between Mg-Al tourmaline and fluid. Contributions to Mineralogy and Petrology 171.

Bocchio R., Adamo I., Bordoni V., Caucia F., Diella V., 2012. Gem-quality zoisite from Merelani (Northeastern Tanzania): Review and new data. Periodico di Mineralogia 81, 379-391.

Bosi F., 2018. Tourmaline crystal chemistry. American Mineralogist 103, 298-306.

Bosi F., Lucchesi S., Reznitskii L., 2004. Crystal chemistry of the dravite-chromdravite series. European Journal of Mineralogy 16, 345-352.

Bosi F., Reznitskii L., Skogby H., 2012. Oxy-chromium-dravite, $NaCr_3(Cr_4Mg_2)(Si_6O_{18})$ $(BO_3)_3(OH)_3O$, a new mineral species of the tourmaline supergroup. American Mineralogist 97, 2024-2030.

Bosi F., Skogby H., Reznitskii L., Hålenius U., 2014. Vanadio-

oxy-dravite, $NaV_3(Al_4Mg_2)(Si_6O_{18})(BO_3)_3(OH)_3O$, a new mineral species of the tourmaline supergroup. American Mineralogist 99, 218-224.

Bosi F., Reznitskii L., Hålenius U. and Skogby H., 2017. Crystal chemistry of Al-V-Cr oxy-tourmalines from Sludyanka complex, Lake Baikal, Russia. European Journal of Mineralogy 29, 457-472.

Bosi F., Biagioni C., Pezzotta F., Skogby H., Hålenius U., Cempírek J., Hawthorne F.C., Lussier A.J., Abdu Y.A., Day M.C., 2022. Uvite, $CaMg_3(Al_5Mg)(Si_6O_{18})(BO_3)_3(OH)_3(OH)$, a new, but long-anticipated mineral species of the tourmaline supergroup from San Piero in Campo, Elba Island, Italy. Mineralogical Magazine 86, 767-776.

Cahen L., 1961. Review of geochronological knowledge in Middle and Northern Africa. Annals of the New York Academy of Sciences 91, 535-566.

Celata B., Ballirano P., Andreozzi G.B., Bosi F., 2021. In situ high-temperature behaviour of fluor-elbaite: breakdown conditions and products. Physics and Chemistry of Minerals 48, 24.

Dingwell D.B., Knoche R., Webb S.L., Pichavant M., 1992. The effect of B_2O_3 on the viscosity of haplogranitic liquids. American Mineralogist 77, 457-461.

Ertl A., Kolitsch U., Dyar M.D., Hughes J.M., Rossman G.R., Pieczka A., Henry D.J., Pezzotta F., Prowatke S., Lengauer C.L., Körner W., Brandstätter F., Francis C.A., Prem M., Tillmanns E., 2012. Limitations of Fe^{2+} and Mn^{2+} site occupancy in tourmaline: Evidence from Fe^{2+}- and Mn^{2+}-rich tourmaline. American Mineralogist 97, 1402-1416.

Feneyrol J., Giuliani G., Ohnenstetter D., Fallick A.E., Martelat J.E., Monié P., Dubessy J., Rollion-Bard C., Le Goff E., Malisa E., Rakotondrazafy A.F.M., Pardieu V., Kahn T., Ichang'i D., Venance E., Voarintsoa N.R., Ranatsenho M.M., Simonet C., Omito E., Nyamai C., Saul M., 2013. New aspects and perspectives on tsavorite deposits. Ore Geology Reviews 53, 1-25.

Filip J., Bosi F., Novák M., Skogby H., Tuček J., Čuda J., Wildner M., 2012. Iron redox reactions in the tourmaline structure: high-temperature treatment of Fe^{3+}-rich schorl. Geochimica et Cosmochimica Acta 86, 239-256.

Gaft M., Reisfeld R., Panczer G., 2005. Modern Luminescence Spectroscopy of Minerals and Materials. Modern Luminescence Spectroscopy of Minerals and Materials. Springer Cham, Heidelberg, 606 pp.

Harris C., Hlongwane W., Gule N., Scheepers R., 2014. Origin of tanzanite and associated gemstone mineralization at Merelani, Tanzania. South African Journal of Geology 117, 15-30.

Hauzenberger C.A., Bauernhofer A.H., Hoinkes G., Wallbrecher E., Mathu E.M., 2004. Pan-African high pressure granulites from SE-Kenya: Petrological and geothermobarometric evidence for a polycyclic evolution in the Mozambique belt. Journal of African Earth Sciences 40, 245-268.

Hauzenberger C.A., Sommer H., Fritz H., Bauerhofer A., Kröner A., Hoinkes G., Wallbrecher E., Thöni M., 2007. SHRIMP U-Pb zircon and Sm-Nd garnet ages from the granulite-facies basement of SE Kenya: Evidence for Neoproterozoic polycyclic assembly of the Mozambique Belt. Journal of the Geological Society 164, 189-201.

Hawthorne F.C., 2002. Bond-valence constraints on the chemical composition of tourmaline. Canadian Mineralogist 40, 789-797.

Hawthorne F.C., MacDonald D.J., Burns P.C., 1993. Reassignment of cation site occupancies in tourmaline: Al-Mg disorder in the crystal structure of dravite. American Mineralogist 78, 265-270.

Henry D.J. and Dutrow B., 1990. Ca substitution in Li-poor aluminous tourmaline. Canadian Mineralogist 28, 111-124.

Henry D.J. and Dutrow B.L., 1996. Metamorphic Tourmaline and Its Petrologic Applications. Reviews in Mineralogy 33, 503-557.

Henry D.J. and Guidotti C.V., 1985. Tourmaline as a petrogenetic indicator mineral: an example from the staurolite-grade metapelites of NW Maine. American Mineralogist 70, 1-15.

Henry D.J., Novák M., Hawthorne F.C., Ertl A., Dutrow B.L., Uher P., Pezzotta F., 2011. Nomenclature of the tourmaline-supergroup minerals. American Mineralogist 96, 895-913.

Kardošová P., Bačík P., Fridrichová J., Celata B., Bosi F., Miglierini M., Mikuš T., Furka D., Furka S., Škoda R., 2024. Crystal-chemical effects of heat treatment on Mg-dominant tourmalines. In press.

Kroner A., 1977. Precambrian mobile belts of Southern and Eastern Africa - ancient sutures or sites of ensialic mobility? A case for crustal evolution towards plate tectonics. Tectonophysics 40, 101-135.

Le Goff E., Deschamps Y., Guerrot C., 2010. Tectonic implications of new single zircon Pb-Pb evaporation data in the Lossogonoi and Longido ruby districts, Mozambican metamorphic Belt of north-eastern Tanzania. Comptes Rendus - Geoscience 342, 36-45.

MacDonald D.J. and Hawthorne F.C., 1995. The crystal chemistry of Si <-> Al substitution in tourmaline. The Canadian Mineralogist 33, 849-858.

Malisa E.P., 1998. Application of graphite as a geothermometer in hydrothermally altered metamorphic rocks of the Merelani-Lelatema area, Mozambique Belt, northeastern Tanzania. Journal of African Earth Sciences 26, 313-316.

Malisa E.P.J., 2004. Trace elements characterization of the hydrothermally deposited tanzanite and green grossular in the Merelani - Lelatema shear zone, northeastern Tanzania. Tanzania Journal of Science 29, 45-60.

Mattson S.M. and Rossman G.R., 1984. Ferric iron in tourmaline. Physics and Chemistry of Minerals 11, 225-234.

Mattson S.M. and Rossman G.R., 1987. Identifying characteristics of charge transfer transitions in minerals. Physics and Chemistry of Minerals 14, 94-99.

Merlet C., 1994. An accurate computer correction program for

quantitative electron probe microanalysis. Microchimica Acta 114-115, 363-376.

Miyashiro A. and Iiyama T., 1954. A Preliminary Note on a New Mineral, Indialite, Polymorphic with Cordierite. Proceedings of the Japan Academy 30, 746-751.

Miyashiro A., Iiyama T., Miyashiro T., Yamasaki M., 1955. The polymorphism of cordierite and indialite. American Journal of Science 253, 185-208.

Muhongo S. and Lenoir J.L., 1994. Pan-African granulite-facies metamorphism in the Mozambique Belt of Tanzania: U-Pb zircon geochronology. Journal of the Geological Society 151, 343-347.

Muhongo S., Tuisku P., Mtoni Y., 1999. Pan-African pressure-temperature evolution of the Merelani area in the Mozambique Belt in northeast Tanzania. Journal of African Earth Sciences 29, 353-365.

Ota T., Kobayashi K., Kunihiro T., Nakamura E., 2008a. Boron cycling by subducted lithosphere; insights from diamondiferous tourmaline from the Kokchetav ultrahigh-pressure metamorphic belt. Geochimica et Cosmochimica Acta 72, 3531-3541.

Ota T., Kobayashi K., Katsura T., Nakamura E., 2008b. Tourmaline breakdown in a pelitic system: Implications for boron cycling through subduction zones. Contributions to Mineralogy and Petrology 155, 19-32.

Pichavant M., 1981. An experimental study of the effect of boron on a water saturated haplogranite at 1 Kbar vapour pressure - Geological applications. Contributions to Mineralogy and Petrology 76, 430-439.

Pohl W. and Niedermayr G., 1979. Geology of the Mwatate Quadrangle and the Vanadium Grossularite Deposits of the Area, 55 p. Nairobi.

Pohl W., Horkel A., Neubauer W., Niedermayr G., Okelo R.E., Wachira J.K., Werneck W., 1980. Notes on the Geology and Mineral Resources of the MtitoAndei-Taita Area (Southern Kenya). Mitteilungender Österreichischen Geologischen Gesellschaft 73, 135-152.

Rumyantseva E. V., 1983. Chromdravite, a new mineral. Zapiski Vsesoyuznogo Mineralogicheskogo Obshchestva 112, 222-226.

Schreyer W., Maresch W.V., Daniels P., Wolfsdorff P., 1990. Potassic cordierites: characteristic minerals for high-temperature, very low-pressure environments. Contributions to Mineralogy and Petrology 105, 162-172.

Scribner E.D., Cempírek J., Groat L.A., James Evans R., Biagioni C., Bosi F., Dini A., Hålenius U., Orlandi P., Pasero M., 2021. Magnesio-lucchesiite, $CaMg_3Al_6(Si_6O_{18})(BO_3)_3(OH)_3O$, a new species of the tourmaline supergroup. American Mineralogist 106, 862-871.

Sęk M.P., Włodek A., Stachowicz M., Woźniak K., Pieczka A., 2023. Magnesio-lucchesiite from the Kowary vicinity, Karkonosze Mountains, SW Poland: the third occurrence worldwide. Mineralogical Magazine 87, 60-68.

Shimizu R. and Ogasawara Y., 2013. Diversity of potassium-bearing tourmalines in diamondiferous Kokchetav UHP metamorphic rocks: A geochemical recorder from peak to retrograde metamorphic stages. Journal of Asian Earth Sciences 63, 39-55.

Steenstra E.S., Klaver M., Berndt J., Flemetakis S., Rohrbach A., Klemme S., 2024. Thermal Stability of F-Rich Phlogopite and K-Richterite During Partial Melting of Metasomatized Mantle Peridotite With Implications for Deep Earth Volatile Cycles. Journal of Geophysical Research: Solid Earth 129, e2023JB028202.

Sun J., Yang Y., Ingrin J., Wang Z., Xia Q., 2022. Impact of fluorine on the thermal stability of phlogopite. American Mineralogist 107, 815-825.

Tartarotti P., Martin S., Meyzen C.M., Benciolini L., Toffolo L., 2019. Structural Evolution and Metasomatism of Subducted Metaophiolites in the Northwestern Alps. Tectonics 38, 4185-4206.